

Numerical modeling of the multi-stage Stern–Gerlach experiment by Frisch and Segrè using co-quantum dynamics via the Bloch equation

Kelvin Titimbo,[†] David C. Garrett,[†] S. Suleyman Kahraman,[†] Zhe He,[†] and Lihong V. Wang*
*Caltech Optical Imaging Laboratory, Andrew and Peggy Cherng Department of Medical Engineering,
Department of Electrical Engineering, California Institute of Technology,
1200 E. California Blvd., MC 138-78, Pasadena, CA 91125, USA*
(Dated: August 30, 2022)

We numerically study the spin flip in the Frisch–Segrè experiment, the first multi-stage Stern–Gerlach experiment, within the context of the novel co-quantum dynamics theory. We model the middle stage responsible for spin rotation by sampling the atoms with the Monte Carlo method and solving the dynamics of the electron and nuclear magnetic moments numerically according to the Bloch equation. Our results show that, without using any fitting parameters, the co-quantum dynamics closely reproduces the experimental observation reported by Frisch and Segrè in 1933, which has so far lacked theoretical predictions.

Keywords: spin-flip transition, electron spin, Bloch equation, co-quantum dynamics.

I. INTRODUCTION

The Stern–Gerlach experiment was a crucial benchmark for the early development of quantum mechanics [1, 2] and is still presented in introductory books as evidence of quantization and the existence of the electron spin angular momentum [3–7]. The so-called Stern–Gerlach apparatus (SG) has been used to illustrate the projection of the quantum wave function onto its eigenstates along the quantization axis, which is given by the direction of a strong inhomogeneous magnetic field. Despite quantum mechanics being fundamental for explaining physical phenomena in almost any branch of physics, there is no generally accepted theory for how the wave function collapses [8–11].

Recently, a novel theory denoted co-quantum dynamics (CQD) has been proposed to describe the evolution and collapse of electron spins in alkali atoms interacting with an external magnetic field, \mathbf{B} [12, 13]. In CQD, the electron magnetic moment μ_e is termed the principal quantum, whereas the nuclear magnetic moment μ_n is termed the co-quantum. The evolution of both quanta is modeled by the Bloch equation, and the collapse of the principal quantum is treated by adding an induction term. In addition to \mathbf{B} , the magnetic field \mathbf{B}_n generated by the nuclear magnetic moment also acts upon μ_e ; similarly, the magnetic field \mathbf{B}_e generated by the electron magnetic moment acts upon μ_n .

We apply CQD to model the multi-stage Stern–Gerlach experiment conducted by R. Frisch and E. Segrè [14]. Their apparatus is composed of two Stern–Gerlach stages and an intervening stage referred to as the inner rotation chamber. The middle stage is characterized by the presence of a weak but rapidly varying magnetic field that rotates the electron magnetic moment. Despite attempts by E. Majorana

[15] and I.I. Rabi [16–18], theoretical descriptions of this experiment deviate from the Frisch–Segrè experimental observation [13, 19]. To date, this divergence remains unresolved by the standard concepts of quantum mechanics [19–21]. However, a closed-form approximation of CQD matches the experimental data with a high coefficient of determination without the use of fitting parameters [13]. The approximation models the dynamics by means of the Schrödinger equation coupled with the CQD concept; this approach has been corroborated numerically [22]. Here, we validate CQD by numerically solving the Bloch equation instead to estimate the fraction of spin flip in the Frisch–Segrè experiment and achieve a high coefficient of determination.

The manuscript is organized as follows. The experimental setup used by Frisch and Segrè is described in Section II. The CQD theory for the experiment is described in Section III. First, we introduce the equations of motion for the electron and nuclear magnetic moments. Second, we describe all stages in the Frisch–Segrè experiment with emphasis on the intermediate stage. We compare our numerical results with both the experimental observation and the analytical solution reported previously [13]. In Section IV, we make final remarks about our findings. In the Appendices, we mathematically derive the approximated external magnetic field (Appendix A) and summarize the closed-form analytical formula obtained using CQD (Appendix B).

II. EXPERIMENT

A schematic of the multi-stage Stern–Gerlach apparatus, first constructed by T.E. Phipps and O. Stern [23] and later improved by Frisch and Segrè [14], is shown in Fig. 1. The experimental setup combines two magnet pairs, SG1 and SG2, which each act as a standard Stern–Gerlach apparatus [2, 7, 24]. Between them, a magnetically shielded inner rotation chamber contains a homogeneous remnant magnetic field and a cylindrically

[†] These authors contributed equally.

* Email:lvw@caltech.edu

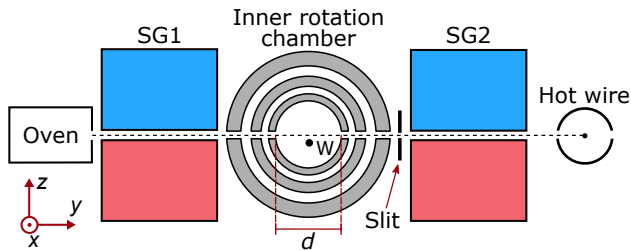


FIG. 1. Schematic of the Frisch–Segrè apparatus as in [14]. The atomic beam from the oven is sent to SG1, whose inhomogeneous magnetic field points along the z -axis. The blue color indicates the magnetic south pole, whereas the red color indicates the magnetic north pole. Then, the atomic beam enters the magnetically shielded inner rotation chamber containing a remnant homogeneous magnetic field plus a magnetic field generated by the electric current I_w flowing through a wire W along the $-x$ -direction. A slit post-selects one of the initially aligned branches of the electron magnetic moment. Finally, the atoms travel through SG2, and the fraction of spin flip is measured using a hot wire.

symmetric magnetic field generated by a current-carrying wire. The aim of the experiment is to observe spin flips in ground-state alkali atoms due to non-adiabatic rotations in the middle stage.

Alkali atoms are appealing for this experiment since their ground state has a closed shell with only one valence electron having an orbital angular momentum $\mathbf{L} = 0$. As a consequence, the total angular momentum for the electron of the atom equals the spin \mathbf{S} , with $S = 1/2$, and the spin–orbit coupling vanishes. However, the electron–nuclear spin interaction, also called the hyperfine interaction, arises from the coupling between the nuclear magnetic moment $\boldsymbol{\mu}_n$ and the magnetic field generated by the electron magnetic moment $\boldsymbol{\mu}_e$, or equivalently vice versa. The coupling strength depends on the relative orientations of the magnetic moments, which are related to the spin angular momenta as

$$\boldsymbol{\mu}_e = \gamma_e \mathbf{S}, \quad \boldsymbol{\mu}_n = \gamma_n \mathbf{I}, \quad (1)$$

where γ_e is the electron gyromagnetic ratio, γ_n is the nuclear gyromagnetic ratio, and \mathbf{I} is the nuclear spin.

A beam of alkali atoms is easily generated since alkali metals have sufficient vapor pressure at temperatures of only a few hundred degrees Celsius [25, 26]. Let us consider the beam of atoms emerging from an oven and propagating along the y direction as shown in Fig. 1. The atomic beam first enters SG1, the strong magnetic field ($\mathbf{B}_0 \sim 0.5$ T) along the z -axis defines the quantization axis. The initially isotropically oriented electron magnetic moments are quickly aligned parallel \uparrow or antiparallel \downarrow to the magnetic field direction. The gradient of the magnetic field deflects the atoms into two branches. Despite no branch being physically selected before the inner rotation chamber, in the following description, we track only the branch with magnetic moments parallel to the field. Figure 2 depicts the general behavior of electron

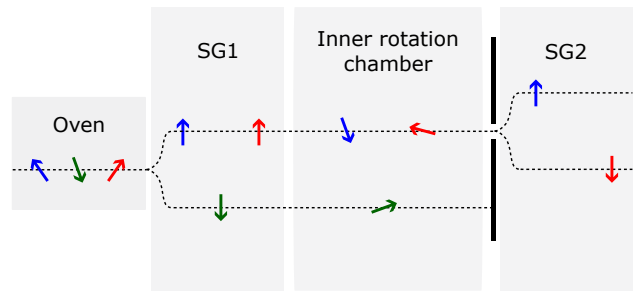


FIG. 2. Illustration of three representative electron magnetic moments of atoms traversing the Frisch–Segrè apparatus. At the oven, the electron magnetic moments are randomly oriented, SG1 aligns them to \uparrow and \downarrow with respect to the orientation of the magnetic field. Both branches enter the inner rotation chamber, where the varying magnetic field rotates the electron magnetic moments. The upper branch is selected using a slit, and the atomic beam is sent to SG2 where the electron magnetic moments are again aligned. Finally, both branches are measured to quantify the fraction of spin flip.

magnetic moments through the experimental setup.

Next, the split beam is sent into an inner rotation chamber, which has an innermost diameter d . Inside the innermost chamber, a weak remnant field $\mathbf{B}_r = B_r \hat{\mathbf{z}}$ remains despite shielding from the fringe fields of SG1 and SG2. A wire with electric current I_w , flowing along the $-x$ direction, is placed at a vertical distance z_a below the atomic beam. Figure 3a shows the main elements and the coordinate system inside the chamber. For an infinitely long straight wire, the magnetic field generated by the current, $\forall y, z$ in the chamber, is given by

$$\mathbf{B}_w = \frac{\mu_0 I_w}{2\pi [(z + z_a)^2 + y^2]} [(z + z_a) \hat{\mathbf{y}} - y \hat{\mathbf{z}}], \quad (2)$$

where μ_0 denotes the vacuum permeability. Therefore, the total field in the innermost shielded region is $\mathbf{B} = \mathbf{B}_w + \mathbf{B}_r$. As illustrated in Fig. 3b, the magnetic field cancels at the null point (NP), at position $\mathbf{r}_{\text{NP}} = y_{\text{NP}} \hat{\mathbf{y}} - z_a \hat{\mathbf{z}}$, with

$$y_{\text{NP}} = \frac{\mu_0 I_w}{2\pi B_r}. \quad (3)$$

In the region near the NP, a first-order Taylor expansion around the point $(y_{\text{NP}}, -z_a)$ approximates the magnetic field as a quadrupole (see Appendix A for details):

$$\mathbf{B} \xrightarrow[\text{vicinity}]{\text{NP}} \mathbf{B}_q = \frac{2\pi B_r^2}{\mu_0 I_w} \left[(z + z_a) \hat{\mathbf{y}} + (y - y_{\text{NP}}) \hat{\mathbf{z}} \right]. \quad (4)$$

After the atom interacts with the field inside the inner rotation chamber, the upper branch is selected using a slit while the lower branch is blocked, as illustrated in Fig. 2. Frisch and Segrè claimed that placing the slit immediately after instead of before the inner rotation chamber improved the beam quality [14].

Finally, the selected atomic branch enters SG2. This second Stern–Gerlach stage again aligns the electron

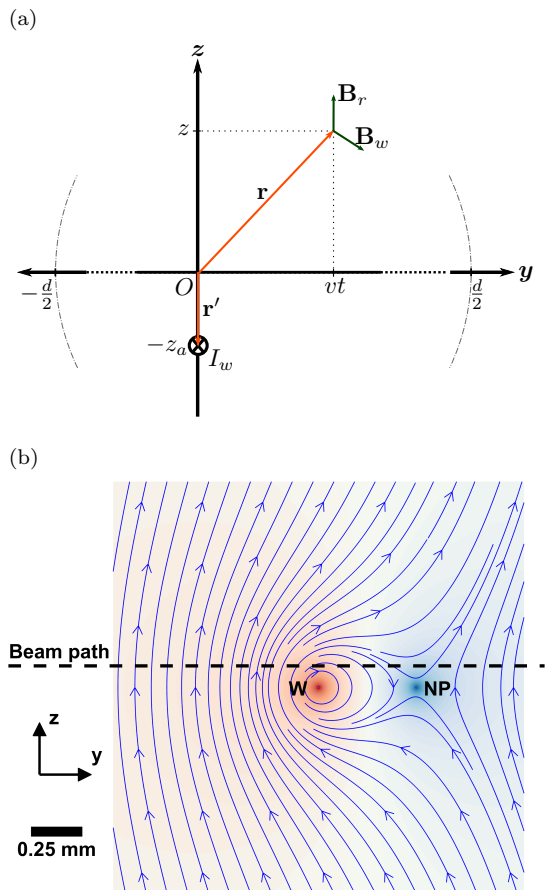


FIG. 3. Magnetic field inside the inner rotation chamber. The beam propagates along the y -axis at constant speed v . The top panel shows the Cartesian reference frame, the position of the current-carrying wire (not drawn to scale), and the contributions from the remnant field \mathbf{B}_r and the wire field \mathbf{B}_w to the total magnetic field at position \mathbf{r} . The bottom panel shows the field lines of the total magnetic field with a null point (NP) below the beam path. In this example from the Frisch–Segrè experiment [14], $B_r = 42 \mu\text{T}$, $I_w = 0.02 \text{ A}$, and $z_a = 105 \mu\text{m}$.

magnetic moment of each atom in parallel \uparrow and antiparallel \downarrow directions. A hot wire records the final distribution of the atoms, which is used to quantify the fraction of spin flip of the electron magnetic moment resulting from the inner rotation chamber. The experiment is repeated with varying wire currents I_w , producing a fraction of spin flip as a function of the current.

III. THEORY

Here, we use CQD [12, 13] to describe the multi-stage Stern–Gerlach experiment by Frisch and Segrè. The formalism provides a mechanism of collapse of the electron spin in atoms interacting with an external magnetic field based on the combined dynamics of the electron and nuclear magnetic moments (1). The Bloch equation governs the evolution of the magnetic moments in the inner rotation chamber.

A. Magnetic moment evolution

The evolution of the magnetic moments in an external magnetic field are described by the Bloch equation [27]:

$$\frac{d\hat{\boldsymbol{\mu}}}{dt} = \gamma \hat{\boldsymbol{\mu}} \times \mathbf{B}, \quad (5)$$

where $\hat{\boldsymbol{\mu}}$ denotes the unit vector of the magnetic moment, γ is the gyromagnetic ratio, and \mathbf{B} is the magnetic flux density. This equation governs an undamped precession of the magnetic moment about the magnetic field \mathbf{B} . While usually considered a classical formalism, the Bloch equation has been recently shown to yield the space-independent von Neumann equation [12].

For the principal quantum $\boldsymbol{\mu}_e$ and the co-quantum $\boldsymbol{\mu}_n$, the Bloch equation (5) becomes

$$\frac{d\hat{\boldsymbol{\mu}}_e}{dt} = \gamma_e \hat{\boldsymbol{\mu}}_e \times (\mathbf{B} + \mathbf{B}_n), \quad (6)$$

$$\frac{d\hat{\boldsymbol{\mu}}_n}{dt} = \gamma_n \hat{\boldsymbol{\mu}}_n \times (\mathbf{B} + \mathbf{B}_e), \quad (7)$$

where γ_e and γ_n denote the gyromagnetic ratios of the electron and the nucleus, respectively, and \mathbf{B} the external magnetic field. CQD introduces the $\boldsymbol{\mu}_e$ – $\boldsymbol{\mu}_n$ interaction via each other’s torque-averaged magnetic field, given by [13]

$$\mathbf{B}_e = \frac{5\mu_0 \mu_e}{16\pi R^3} \hat{\boldsymbol{\mu}}_e = B_e \hat{\boldsymbol{\mu}}_e, \quad (8)$$

$$\mathbf{B}_n = \frac{5\mu_0 \mu_n}{16\pi R^3} \hat{\boldsymbol{\mu}}_n = B_n \hat{\boldsymbol{\mu}}_n, \quad (9)$$

where R is the van der Waals radius of the atom, and μ_e and μ_n are the magnitudes of the magnetic moments for the electron and the nucleus, respectively.

The orientations of the magnetic moments in \mathbb{R}^3 are conveniently described using spherical coordinates. With the polar and azimuthal angles, θ_e and ϕ_e for $\boldsymbol{\mu}_e$ and θ_n and ϕ_n for $\boldsymbol{\mu}_n$, we write the unit vectors as

$$\hat{\boldsymbol{\mu}}_e = \begin{pmatrix} \sin(\theta_e) \cos(\phi_e) \\ \sin(\theta_e) \sin(\phi_e) \\ \cos(\theta_e) \end{pmatrix}, \quad (10)$$

$$\hat{\boldsymbol{\mu}}_n = \begin{pmatrix} \sin(\theta_n) \cos(\phi_n) \\ \sin(\theta_n) \sin(\phi_n) \\ \cos(\theta_n) \end{pmatrix}. \quad (11)$$

Meanwhile, the external field is written as

$$\mathbf{B} = \begin{pmatrix} B_x \\ B_y \\ B_z \end{pmatrix}. \quad (12)$$

Finally, substituting (8)–(12) into (6) and (7), we obtain a set of differential equations determining the evolution of the unit vectors of $\boldsymbol{\mu}_e$ and $\boldsymbol{\mu}_n$:

$$\dot{\theta}_e = -\gamma_e [B_y \cos(\phi_e) - B_x \sin(\phi_e) + B_n \sin(\theta_n) \sin(\phi_n - \phi_e)] , \quad (13a)$$

$$\dot{\phi}_e = -\gamma_e [B_z + B_n \cos(\theta_n) - \cot(\theta_e) [B_x \cos(\phi_e) + B_y \sin(\phi_e) + B_n \sin(\theta_n) \cos(\phi_e - \phi_n)]] , \quad (13b)$$

$$\dot{\theta}_n = -\gamma_n [B_y \cos(\phi_n) - B_x \sin(\phi_n) + B_e \sin(\theta_e) \sin(\phi_e - \phi_n)] , \quad (13c)$$

$$\dot{\phi}_n = -\gamma_n [B_z + B_e \cos(\theta_e) - \cot(\theta_n) [B_x \cos(\phi_n) + B_y \sin(\phi_n) + B_e \sin(\theta_e) \cos(\phi_e - \phi_n)]] . \quad (13d)$$

Given the dynamical equations for the electron and nuclear magnetic moments of a single atom, we model their evolution in the inner rotation chamber of the Frisch–Segrè experiment.

B. Multi-stage Stern–Gerlach experiment by Frisch and Segrè

In the Frisch–Segrè experiment, neutral potassium-39 atoms (^{39}K) with an electron configuration of $[\text{Ar}] 4s^1$ were used. The valence electron in its ground state is fully specified in the Russell-Saunders notation as $4^2S_{1/2}$. Table I lists the values of the van der Waals radius, spins, magnetic moments, and gyromagnetic ratios for the ^{39}K atom. Accordingly, we compute the magnitudes of the magnetic fields generated by the electron and nuclear magnetic moments from (8) and (9):

$$B_e = 55.806\,267\,22(2) \text{ mT}, \quad (14a)$$

$$B_n = 11.8842(3) \text{ } \mu\text{T} . \quad (14b)$$

1. Oven

First, heating ^{39}K atoms in an oven with a small opening produces an effusive beam of non-interacting thermal atoms. We define the y -axis along the beam as shown in Fig. 1.

The initial orientations of both the electron and nuclear magnetic moments of a single traveling atom are

TABLE I. Values for potassium-39 [28–32].

		^{39}K	
		Property	Value
Atom		R	275 pm
Valence electron		S	$\frac{1}{2}$
		μ_e	$9.284\,767\,704\,3(28) \times 10^{-24} \text{ J/T}$
		γ_e	$-1.760\,859\,630\,23(53) \times 10^{11} \text{ rad/(s T)}$
Nucleus		I	$\frac{3}{2}$
		μ_n	$1.977\,23(4) \times 10^{-27} \text{ J/T}$
		γ_n	$1.250\,061\,2(3) \times 10^7 \text{ rad/(s T)}$

isotropically distributed. Therefore, their angular probability density functions are respectively

$$p_{e,\text{oven}}(\theta_{e,\text{oven}}, \phi_{e,\text{oven}}) = \frac{1}{4\pi},$$

$$p_{n,\text{oven}}(\theta_{n,\text{oven}}, \phi_{n,\text{oven}}) = \frac{1}{4\pi} .$$

To implement a Monte Carlo simulation, the polar and azimuthal angles are numerically generated from independent realizations of

$$\theta_{e,\text{oven}} = 2 \arcsin(\sqrt{\zeta_1}), \quad \phi_{e,\text{oven}} = 2\pi\zeta_2, \quad (15)$$

$$\theta_{n,\text{oven}} = 2 \arcsin(\sqrt{\zeta_3}), \quad \phi_{n,\text{oven}} = 2\pi\zeta_4, \quad (16)$$

with ζ_j , $j = 1, \dots, 4$, being random numbers uniformly sampled from zero to one.

2. Stern–Gerlach apparatus 1

Emerging from the oven, the atoms enter a Stern–Gerlach apparatus consisting of an inhomogeneous magnetic field with a strong gradient along the z -axis, as illustrated in Fig. 1. Usually, the amplitude of the magnetic field is $B_0 \sim 0.5 \text{ T}$; thus, $B_0 > B_e \gg B_n$. For such a strong field, $\boldsymbol{\mu}_e$ and $\boldsymbol{\mu}_n$ couple more strongly to the external magnetic field than to each other, and can be considered as independently precessing with Larmor frequencies ω_e and ω_n , for electron and nuclear magnetic moments, respectively, about the external field direction. From the values in Table I, the ratio between the nuclear and electron Larmor frequencies $\omega_n/\omega_e \approx 7 \times 10^{-5}$. In consequence, while the flight time guarantees the collapse of the electron magnetic moment, it is too short for the nuclear magnetic moment to collapse [13].

Therefore, the electron magnetic moments of the single atoms, initially isotropically distributed, split into two branches with well-defined opposite alignments along the z -axis. We characterize the orientations of the aligned $\boldsymbol{\mu}_e$ by setting $\theta_{e,0} = 0$ and $\theta_{e,0} = \pi$ in (10), respectively, as illustrated in Fig. 2. Meanwhile, since $\boldsymbol{\mu}_n$ does not collapse, CQD assumes that θ_n does not vary significantly during the flight. CQD shows that at the end of the SG1 stage, the $\boldsymbol{\mu}_n$ orientation in each of the branches is redistributed into an anisotropic probability density

function [13]:

$$p_n(\theta_{n,0}, \phi_{n,0}) = \begin{cases} \frac{1}{4\pi} (1 - \cos(\theta_{n,0})) & \text{if } \theta_{e,0} = 0, \\ \frac{1}{4\pi} (1 + \cos(\theta_{n,0})) & \text{if } \theta_{e,0} = \pi. \end{cases} \quad (17)$$

3. Inner rotation chamber

The inner rotation chamber consists of three hollow iron shielding spheres. Without shielding, the fringe field was ~ 0.4 T; with shielding, the remnant field along the $+z$ -axis was measured as $B_r = 42 \mu\text{T}$ [14]. Inside the chamber, an electric current I_w flowing through a wire produces a spatially varying magnetic field (2), resulting in the total field shown in Fig. 3b.

We select the branch of the atomic beam with μ_e aligned to the $+z$ -axis, *i.e.*, $\theta_{e,0} = 0$, as shown in Fig. 2. Therefore, the probability density function (17) becomes

$$p_n(\theta_{n,0}, \phi_{n,0}) = \frac{1}{4\pi} (1 - \cos(\theta_{n,0})). \quad (18)$$

To continue the Monte Carlo simulation, the polar and azimuthal angles $(\theta_{n,0}, \phi_{n,0})$ are sampled from the above anisotropic probability density function:

$$\theta_{n,0} = 2 \arcsin(\zeta_1^{1/4}), \quad \phi_{n,0} = 2\pi \zeta_2, \quad (19)$$

where ζ_1 and ζ_2 are two independent random numbers sampled uniformly from zero to one.

Each atom in the beam propagates with velocity $\mathbf{v} = v \hat{\mathbf{y}}$, and we approximate the motion to be rectilinear and uniform such that its position on the propagation axis is $y = vt$. The atom is simulated from $-d/2$ to $d/2$ as shown in Fig. 3a. Here, $v = 800$ m/s and $d = 16.3$ mm [14]. Therefore, the time in the inner rotation chamber $t \in [-10.2 \mu\text{s}, 10.2 \mu\text{s}]$. The total magnetic field along the y -axis varies according to

$$\mathbf{B} = \frac{\mu_0 I_w}{2\pi [z_a^2 + (vt)^2]} [z_a \hat{\mathbf{y}} - vt \hat{\mathbf{z}}] + B_r \hat{\mathbf{z}}. \quad (20)$$

The wire is positioned along the x -axis at a distance $z_a = 105 \mu\text{m}$ below the beam path. The electric current I_w varies from 0.01 A to 0.5 A [14].

It is known that a time-dependent magnetic field can rotate the magnetic moment of the electron [15, 18]. To determine whether the process is adiabatic or non-adiabatic, we compute the so-called adiabaticity parameter, defined as the ratio between the absolute values of the Larmor frequency ω_e and the rotational speed of the field in the yz plane Ω_B [15]:

$$k = \left| \frac{\omega_e}{\Omega_B} \right| = \left| \frac{\gamma_e B}{\frac{d}{dt} [\arctan(B_z/B_y)]} \right|. \quad (21)$$

If $\omega_e \gg \Omega_B$ ($k \gg 1$), μ_e is able to follow the changing orientation of the magnetic field, and the rotation is said

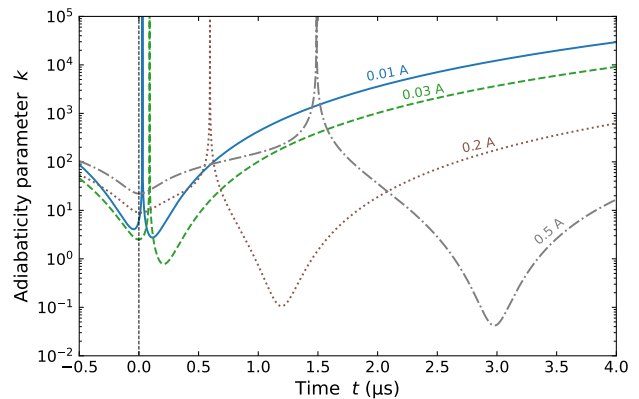


FIG. 4. Adiabaticity parameter k along the beam path for various electric currents. Adiabatic rotation of the electron magnetic moment occurs around the peak ($k \gg 1$), whereas non-adiabatic rotation happens around the trough (near the null point t_{NP} of the magnetic field). The vertical black dashed line indicates the time when the atom is above the wire ($t = 0$).

to be adiabatic. Otherwise, μ_e may be unable to follow the changing orientation of the magnetic field; if so, the rotation is said to be non-adiabatic.

From (20), the adiabaticity parameter becomes

$$k = \left| \frac{\gamma_e \mu_0 I_w}{2\pi z_a v} \frac{\sqrt{(vt)^2 + z_a^2}}{\left(1 - \frac{4\pi B_r vt}{\mu_0 I_w}\right)} \times \left[1 - \frac{4\pi B_r vt}{\mu_0 I_w} + \left(\frac{2\pi B_r}{\mu_0 I_w}\right)^2 ((vt)^2 + z_a^2) \right]^{3/2} \right|. \quad (22)$$

Figure 4 shows the variation of k around the center of the cavity computed from (22) for a set of representative electric currents I_w .

We note that in the vicinity of the wire position ($t = 0$) and before the atoms reach the null point at time

$$t_{\text{NP}} = \frac{y_{\text{NP}}}{v} = \frac{\mu_0 I_w}{2\pi v B_r}, \quad (23)$$

the adiabaticity parameter is much greater than unity at the peaks. Accordingly, as the z component of the magnetic field changes its orientation (see Fig. 3), the electron magnetic moment follows the varying \mathbf{B} -field adiabatically. Therefore, the electron magnetic moment flips adiabatically, $\theta_{e,0} : 0 \mapsto \pi$, in this region. In comparison, Majorana stated that the flip is due to the orientation reversal of the quadrupole field along the flight path [15]. For simplicity, we ignore the contribution from the nucleus (14b) to k because its much weaker field does not significantly affect the magnitudes of the adiabatic peaks in Fig. 4

Then, the electron magnetic moment is rotated non-adiabatically around the corresponding trough in Fig. 4, which is near the null point. We make use of the

quadrupole approximation for the magnetic field to describe this effect near the null point, \mathbf{B}_q in (4), rewritten for the beam path as

$$B_x = 0, \quad (24a)$$

$$B_y = \frac{2\pi B_r^2}{\mu_0 I_w} z_a, \quad (24b)$$

$$B_z = \frac{2\pi B_r^2}{\mu_0 I_w} v(t - t_{\text{NP}}). \quad (24c)$$

The resulting system of coupled differential equations is reduced to

$$\dot{\theta}_e = -\gamma_e [B_y \cos(\phi_e) + B_n \sin(\theta_n) \sin(\phi_n - \phi_e)], \quad (25a)$$

$$\dot{\phi}_e = -\gamma_e [B_z + B_n \cos(\theta_n) - \cot(\theta_e) [B_y \sin(\phi_e) + B_n \sin(\theta_n) \cos(\phi_e - \phi_n)]], \quad (25b)$$

$$\dot{\theta}_n = 0, \quad (25c)$$

$$\dot{\phi}_n = -\gamma_n [B_z + B_e \cos(\theta_e) - \cot(\theta_n) [B_y \sin(\phi_n) + B_e \sin(\theta_e) \cos(\phi_e - \phi_n)]]. \quad (25d)$$

Note that we have imposed the condition $\dot{\theta}_n = 0$ since the postulates of the CQD theory require small variations of the polar angle of the nuclear magnetic moment. This condition corresponds to the selection rule for nuclear spin transitions $\Delta m_I = 0$ [13, 33].

To solve the above differential equations, we sample the initial orientation of $\boldsymbol{\mu}_n$ from (19) and sample $\phi_{e,0}$ uniformly, in a way similar to (15), while setting $\theta_{e,0} = \pi$. The concurrence of two vastly different time scales, $\omega_n/\omega_e \approx 7 \times 10^{-5}$, for the dynamics of $\hat{\boldsymbol{\mu}}_e$ and $\hat{\boldsymbol{\mu}}_n$, leads to stiffness prone to numerical instability [34, 35]. We chose the Radau methods [36, 37] implemented in Julia [38, 39] to solve the differential equations (25) numerically. Our source code is posted online [40]. An alternative approach, to avoid the stiffness, approximates the nuclear Larmor frequency as a constant and accelerates the solution using a variable transformation [22]

Figure 5 shows the characteristic dynamics of θ_e inside the inner rotation chamber for a representative set of currents. To facilitate comparison, we introduce $\Delta t = t - t_{\text{NP}}$, such that the time $\Delta t = 0$ at the current-dependent null point (23). The dynamics are characterized by an oscillatory behavior; the polar angle θ_e varies rapidly in the vicinity of the null point ($\Delta t = 0$) due to strong non-adiabatic rotation. Then, the oscillations are damped due to the increasing adiabaticity parameter for $\Delta t > 0$. However, since θ_e has not asymptotically converged to a definite value, we numerically approximate its final value $\theta_{e,f}$ by averaging the oscillations over the last 2 μs .

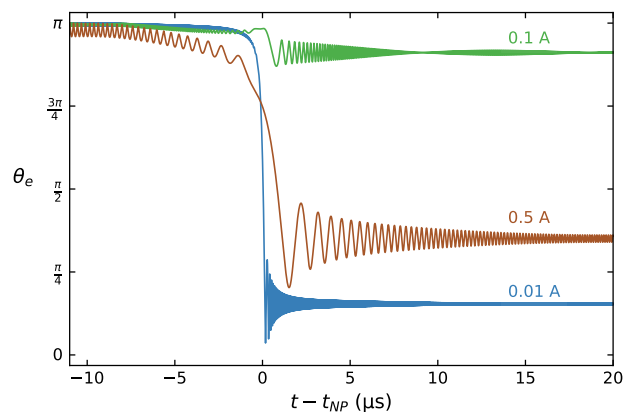


FIG. 5. Dynamics of θ_e for different electric currents I_w . The initial conditions are $\theta_{e,0} = \pi$ and $\phi_{e,0} = 0$ for the electron magnetic moment, whilst $\theta_{n,0} = \frac{5}{8}\pi$ and $\phi_{n,0} = \frac{11}{10}\pi$ for the nuclear magnetic moment.

4. Stern–Gerlach apparatus 2

After traveling through the inner rotation chamber, the atom enters the second Stern–Gerlach apparatus as shown in Fig. 1. The strong magnetic field along the z -axis realigns the electron magnetic moment. The final orientation $\theta_{e,f} \mapsto \theta_{e,D}$ follows the branching condition postulated by the CQD theory [13]:

$$\theta_{e,D} = \begin{cases} 0 & \text{if } \theta_{e,f} < \theta_{n,0}, \\ \pi & \text{if } \theta_{e,f} > \theta_{n,0}. \end{cases} \quad (26)$$

Therefore, the measured polar angle $\theta_{e,D}$ takes on either 0 or π .

5. Fraction of spin flip

The spin flip corresponds to those atoms with $\theta_{e,D} = \pi$, as depicted in Fig. 2. We numerically solved the Bloch equations for $N = 15000$ atoms for each current I_w . Thus, the fraction of spin flip, for a given I_w , is computed using

$$\mathcal{W}_{\text{num}} = \frac{1}{N} \sum_{i=1}^N [\theta_{e,D}^{(i)} = \pi], \quad (27)$$

where i denotes the i th-atom sampled and $[P]$ is the Iverson bracket, which is defined to take on the value 1 when the statement P is true and 0 otherwise.

Figure 6 shows the resulting fraction of spin flip obtained from the numerical simulation in comparison with the experimental results reported by Frisch and Segrè [14]. In addition, the closed-form analytical prediction from the CQD theory is included (see Appendix B) [13].

The coefficient of determination for our numerical simulation is $R_{\text{num}}^2 = 0.945$, compared with $R_{\text{ana}}^2 = 0.962$

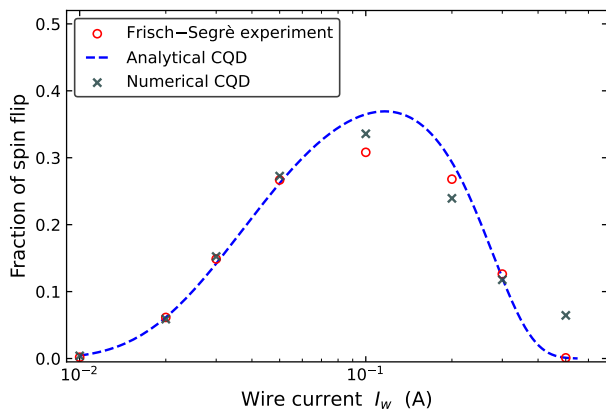


FIG. 6. Fraction of spin flip for the multi-stage Stern–Gerlach experiment by Frisch and Segrè. The red circles are the experimental data [14], the blue dashed line is the closed-form analytical solution from CQD [13], and the gray crosses show the numerical solution from CQD.

from the analytical solution [13]. The statistical errors associated with the numerical results are smaller than the symbol size in Fig. 6. These results show a close agreement of CQD with the experimental data [14], which has not yet been achieved using standard quantum mechanical treatments [21].

IV. CONCLUSIONS

We used CQD to numerically model the Frisch–Segrè experiment without using any fitting parameters. The numerical problem is stiff because of the two vastly different characteristic time scales [13]. The solver of the differential equations must be carefully chosen and validated. We described all the stages of the experiment, with emphasis on the inner rotation chamber. Using the Monte Carlo method, we sampled the spatial orientations of the electron and nuclear magnetic moments of the atoms in the atomic beam. Our findings show that the fraction of spin flip obtained by means of CQD closely reproduces the reported experimental results, with a coefficient of determination of $R_{\text{num}}^2 = 0.945$. The obtained results have not been explained by standard quantum mechanical approaches [21], despite attempts by Majorana [15] and Rabi [16–18], whose theoretical formulae deviate from the experimental results.

Hence, this work supports CQD as a model for both the evolution and the collapse of the electron spin in atoms in the presence of external magnetic fields. Some other reported experiments involving multi-stage Stern–Gerlach experiments [41, 42] could be explored using the present formalism. Notwithstanding, we hope that this work will encourage further experiments to verify CQD.

ACKNOWLEDGMENTS

This project has been made possible in part by grant number 2020-225832 from the Chan Zuckerberg Initiative DAF, an advised fund of the Silicon Valley Community Foundation.

SUPPLEMENTAL MATERIAL

Our source code written in Julia is available online [40].

Appendix A: Approximation to quadrupole field

The total magnetic field inside the inner rotation chamber, $\mathbf{B} = \mathbf{B}_w + \mathbf{B}_r$, can be approximated as an ideal quadrupole field. The Taylor expansion of \mathbf{B} in the yz plane around the null point $(y_{\text{NP}}, -z_a)$ reads

$$\begin{aligned} \mathbf{B} = \mathbf{B} \Big|_{\text{NP}} + \frac{\partial \mathbf{B}}{\partial y} \Big|_{\text{NP}} (y - y_{\text{NP}}) + \frac{\partial \mathbf{B}}{\partial z} \Big|_{\text{NP}} (z + z_a) \\ + \frac{1}{2} \frac{\partial^2 \mathbf{B}}{\partial y^2} \Big|_{\text{NP}} (y - y_{\text{NP}})^2 + \frac{1}{2} \frac{\partial^2 \mathbf{B}}{\partial z^2} \Big|_{\text{NP}} (z + z_a)^2 \\ + \frac{\partial^2 \mathbf{B}}{\partial y \partial z} \Big|_{\text{NP}} (y - y_{\text{NP}})(z + z_a) + \dots \quad (\text{A1}) \end{aligned}$$

Up to the first order, for the hyperbolic field approximation, the coefficients are

$$\mathbf{B} \Big|_{\text{NP}} = 0, \quad (\text{A2a})$$

$$\frac{\partial \mathbf{B}}{\partial y} \Big|_{\text{NP}} = \frac{2\pi B_r^2}{\mu_0 I_w} \hat{\mathbf{z}}, \quad (\text{A2b})$$

$$\frac{\partial \mathbf{B}}{\partial z} \Big|_{\text{NP}} = \frac{2\pi B_r^2}{\mu_0 I_w} \hat{\mathbf{y}}. \quad (\text{A2c})$$

Substituting (A2) into (A1), the quadrupole magnetic field can be written as

$$\mathbf{B}_q = \frac{2\pi B_r^2}{\mu_0 I_w} (z + z_a) \hat{\mathbf{y}} + \frac{2\pi B_r^2}{\mu_0 I_w} (y - y_{\text{NP}}) \hat{\mathbf{z}}. \quad (\text{A3})$$

This corresponds to the magnetic field in (4).

Appendix B: Closed-form solution of the co-quantum dynamics theory

Using the CQD theory, it is possible to derive a closed-form formula for the probability of spin flip in the inner rotation chamber in the presence of the quadrupole magnetic field and the nuclear magnetic moment as we described for the experiment conducted by Frisch and Segrè [13].

In terms of the parameters of the experiment, the fraction of spin flip, shown as the blue dashed line in Fig. 6,

is given by

$$\mathcal{W}_{\text{ana}}(I_w) = \exp \left[-\sqrt{\left(\frac{c_{r0}}{I_w}\right)^2 + c_{rs}^2} - c_{rr} I_w^3 \right], \quad (\text{B1})$$

where

$$c_{r0} = |\gamma_e| \frac{2\pi^2 z_a^2}{\mu_0 v} (B_r + B_n \cos(\langle \theta_n \rangle))^2, \quad (\text{B2a})$$

$$c_{rs} = |\gamma_e| \frac{\pi z_a}{v} B_n \sin(\langle \theta_n \rangle), \quad (\text{B2b})$$

$$c_{rr} = \frac{\mu_0^3 \gamma_e^2 \gamma_n}{32\pi v^3} \frac{B_e (B_n \sin(\langle \theta_n \rangle))^5}{(B_r + B_n \cos(\langle \theta_n \rangle))^6}. \quad (\text{B2c})$$

The coefficients represent three physical effects identified in the solution, *i.e.*, null-point rotation, rotation saturation, and resonant rotation, respectively. The mean polar angle of the nuclear magnetic moment is computed from the probability density function (18) as follows:

$$\langle \theta_n \rangle = \int d\theta_n d\phi_n \sin(\theta_n) p_n(\theta_n, \phi_n) = \frac{5}{8}\pi. \quad (\text{B3})$$

-
- [1] W. Gerlach and O. Stern, Der experimentelle nachweis des magnetischen moments des silberatoms, *Z. Phys.* **8**, 110 (1922).
- [2] W. Gerlach and O. Stern, Über die richtungsquantelung im magnetfeld, *Ann. Phys.* **379**, 673 (1924).
- [3] G. Uhlenbeck and S. Goudsmit, Ersetzung der hypothese vom unmechanischen zwang durch eine forderung bezüglich des inneren verhaltens jedes einzelnen elektrons, *Naturwissenschaften* **13**, 953 (1925).
- [4] I. Estermann, History of molecular beam research: Personal reminiscences of the important evolutionary period 1919–1933, *Am. J. Phys.* **43**, 661 (1975).
- [5] B. H. Bransden and C. J. Joachain, *Physics of Atoms and Molecules* (Longman, 1990).
- [6] W. Greiner, *Quantum Mechanics: An Introduction*, 4th ed. (Springer, 2001).
- [7] A. Messiah, *Quantum Mechanics* (Dover Publications, Inc, 2014).
- [8] E. P. Wigner, The problem of measurement, *Am. J. Phys.* **31**, 6 (1963).
- [9] P. Busch, P. J. Lahti, and P. Mittelstaedt, *The Quantum Theory of Measurement* (Springer, 1996).
- [10] M. Schlosshauer, Decoherence, the measurement problem, and interpretations of quantum mechanics, *Rev. Mod. Phys.* **76**, 1267 (2005).
- [11] A. Bassi, K. Lochan, S. Satin, T. P. Singh, and H. Ulbricht, Models of wave-function collapse, underlying theories, and experimental tests, *Rev. Mod. Phys.* **85**, 471 (2013).
- [12] L. V. Wang, Derivation from Bloch equation to von Neumann Equation to Schrödinger–Pauli equation, *Found. Phys.* **52**, 61 (2022).
- [13] L. V. Wang, Multi-stage Stern-Gerlach experiment modeled (2022), 2208.06471 [quant-ph].
- [14] R. Frisch and E. Segrè, Über die einstellung der richtungsquantelung. II, *Z. Phys.* **80**, 610 (1933).
- [15] E. Majorana, Atomi orientati in campo magnetico variabile, *Il Nuovo Cimento* **9**, 43 (1932).
- [16] I. I. Rabi, On the process of space quantization, *Phys. Rev.* **49**, 324 (1936).
- [17] I. I. Rabi, Space quantization in a gyrating magnetic field, *Phys. Rev.* **51**, 652 (1937).
- [18] F. Bloch and I. I. Rabi, Atoms in variable magnetic fields, *Rev. Mod. Phys.* **17**, 237 (1945).
- [19] H. Schmidt-Böcking, L. Schmidt, H. J. Lüdde, W. Trageser, A. Templeton, and T. Sauer, The Stern–Gerlach experiment revisited, *Eur. Phys. J. H* **41**, 327 (2016).
- [20] B. Friedrich and H. Schmidt-Böcking, eds., *Molecular Beams in Physics and Chemistry: From Otto Stern’s Pioneering Exploits to Present-Day Feats* (Springer, 2021).
- [21] S. S. Kahraman, K. Titimbo, Z. He, J.-T. Shen, and L. V. Wang, Quantum mechanical modeling of the multi-stage Stern–Gerlach experiment by Frisch and Segre via the von Neuman equation, arxiv (2022).
- [22] Z. He, K. Titimbo, S. S. Kahraman, D. Garrett, and L. V. Wang, Numerical modeling of the multi-stage Stern–Gerlach experiment by Frisch and Segrè using co-quantum dynamics via the Schrödinger equation, arxiv (2022).
- [23] T. E. Phipps and O. Stern, Über die einstellung der richtungsquantelung, *Z. Phys.* **73**, 185 (1932).
- [24] D. F. Styer, *The Strange World of Quantum Mechanics* (Cambridge University Press, 2000).
- [25] E. F. Fiock and W. H. Rodebush, The vapor pressures and thermal properties of potassium and some alkali halides, *J. Am. Chem. Soc.* **48**, 2522 (1926).
- [26] C. B. Alcock, V. P. Itkin, and M. K. Horrigan, Vapour pressure equations for the metallic elements: 298–2500K, *Can. Metall. Q.* **23**, 309 (1984).
- [27] F. Bloch, Nuclear induction, *Phys. Rev.* **70**, 460 (1946).
- [28] E. Arimondo, M. Inguscio, and P. Violino, Experimental determinations of the hyperfine structure in the alkali atoms, *Rev. Mod. Phys.* **49**, 31 (1977).
- [29] A. Antušek, D. Kędziera, A. Kaczmarek-Kędziera, and M. Jaszuński, Coupled cluster study of NMR shielding of alkali metal ions in water complexes and magnetic moments of alkali metal nuclei, *Chem. Phys. Lett.* **532**, 1 (2012).
- [30] N. Stone, *Table of Recommended Nuclear Magnetic Dipole Moments*, Tech. Rep. INDC(NDS)–0794 (Nuclear Data Services, International Atomic Energy Agency (IAEA), 2019).
- [31] E. Tiesinga, P. J. Mohr, D. B. Newell, and B. N. Taylor, CODATA recommended values of the fundamental physical constants: 2018, *Rev. Mod. Phys.* **93**, 025010 (2021).
- [32] J. R. Rumble, ed., *CRC Handbook of Chemistry and Physics*, 103rd ed. (CRC Press/Taylor & Francis, 2022).
- [33] A. Barra and A. Hassan, Electron Spin Resonance, in *Encyclopedia of Condensed Matter Physics* (Elsevier, 2005) pp. 58–67.
- [34] R. Aiken, ed., *Stiff Computation* (Oxford University Press, 1985).

- [35] E. Hairer and G. Wanner, *Solving Ordinary Differential Equations II* (Springer, 1996).
- [36] E. Hairer and G. Wanner, Stiff differential equations solved by Radau methods, *J. Comput. Appl. Math.* **111**, 93 (1999).
- [37] M. Darvishi, F. Khani, and A. Soliman, The numerical simulation for stiff systems of ordinary differential equations, *Comput. Math. Appl.* **54**, 1055 (2007).
- [38] C. Rackauckas and Q. Nie, Differentialequations.jl -A performant and feature-rich ecosystem for solving differential equations in Julia, *J. Open Res. Software* **5**, <http://doi.org/10.5334/jors.151> (2017).
- [39] J. Bezanson, A. Edelman, S. Karpinski, and V. B. Shah, Julia: A fresh approach to numerical computing, *SIAM Rev.* **59**, 65 (2017).
- [40] K. Titimbo, D. C. Garrett, S. S. Kahraman, Z. He, and L. V. Wang, Numerical computation of the fraction of spin flip in the Frisch-Segrè experiment using co-quantum dynamics theory, GitHub (2022).
- [41] W. Schröder and G. Baum, A spin flipper for reversal of polarisation in a thermal atomic beam, *J. Phys. E: Sci. Instrum.* **16**, 52 (1983).
- [42] R. D. Hight, R. T. Robiscoe, and W. R. Thorson, Nonadiabatic spin transitions in an inhomogeneous magnetic field, *Phys. Rev. A* **15**, 1079 (1977).